Experimental and computational study into the onset of light damage of Dutch masonry structures

P.A. Korswagen, M. Longo, J.G. Rots

Department of Materials, Mechanics, Management and Design, Delft University of Technology, the Netherlands (p.a.korswagen@tudelft.nl)

In recent decades, extraction of natural gas in the northern part of the Netherlands has resulted in low-magnitude, shallow earthquakes. Besides assessing the safety and 'near collapse' state of the structures in the region, the lower damage state or Damage State 1, is important. Light, repeating, seismic events may cause cracks in masonry houses. This has led to societal unrest, serviceability losses and troubled claiming procedures against the government and the companies involved.

An experimental and computational campaign, ongoing at the Delft University of Technology over the past years, aimed to improve the knowledge of the underlying physics of crack initiation and propagation in typical, unreinforced masonry structures, ubiquitous in the Netherlands. Herein is an overview of this study. First a scalar damage parameter is matched to a damage scale to objectively quantify cracking damage and its progression as a function of crack width, length and number. Next, cracking is observed experimentally in walls and spandrels subjected to in-plane loading using high-resolution Digital Image Correlation to detect the formation and evolution of cracks. The experimental results are then interpreted to establish drift intervals for which light damage can be expected.

Subsequently, orthotropic composite continuum models were calibrated against the test results. Modelling and constitutive improvements were made in these 2D models. Then, the validated models were extrapolated to real building cases, also included herein. The combination of existing damage due to e.g. differential settlement, and new damage due to the seismicity is evaluated with these extrapolation models. Finally, the models provide a relationship between the variability in e.g. material strength, earthquake intensity, and damage; this is then employed to determine probabilities for light damage.

Keywords: Damage, unreinforced masonry, nonlinear finite element analysis, cracking, experimental tests

1 Introduction

The extraction of natural gas in the north of the Netherlands has led to induced seismic events that have been linked to damage to the buildings in the region [1]. The possibility of strong earthquakes, capable of generating severe structural damage, led in tum to an extensive study and characterisation of the (potential) events and the ultimate-limit-state resistance of the exposed structures as detailed for instance in van Elk et al. [2], who discuss the multiple steps between assessing seismicity and building fragility; Messali et al. [3], who present a multi-scale approach towards characterising the ultimate limit state of Dutch masonry structures; Esposito et al. [4], who performed quasi static pushover tests on a full scale clay masonry structure; or Graziotti et al. [5], who conducted dynamic tests of similar structures. Nonetheless, the more frequent, lighter events, occurred to date and likely to occur in the future, are most to blame for the economic losses, societal unrest, and, what can be denoted, 'light damage' to the vulnerable, unreinforced masonry structures, common in the region. The serviceability limit state of these structures requires thus further study.

The Dutch masonry structures, with slender walls, large openings, simple connections, and no seismic- design, are sufficiently unique that no comparable structures are found in other seismic countries. Moreover, the high sensitivity of the ‘light damage’ to the material properties, structural configuration, repeated vibrations, and existing conditions, such as prior (differential) settlement deformations, make the evaluation of the damage more complex. Furthermore, unlike near-collapse assessments, where the characterisation of the damage can be performed using a parameter linked to structural behaviour, such as inter-storey drift, the characterisation of 'light damage' is more aesthetic and can be highly dependent on the progression of the damage due to multiple seismic events. Some studies [6, 7, 8] do observe and categorise damage, but don't consider its propagation in quantifiable detail.

It is in this context that a study into the serviceability behaviour of Dutch masonry and the initiation and progression of ‘light damage’ has been conducted in the past years at the Delft University of Technology. Presented herein is a summary of the main observations regarding light damage as obtained from this study concerning experimental tests and computational finite element models and simulations.

First, however, a few limitations must be mentioned. Foremost, a simultaneous field-case-based study into the origins of the damage [9], revealed that existing damage seemed to be limited to in-plane actions. Therefore, the investigations into light damage have focused so far only on in-plane actions and 2D effects. While out-of-plane actions are extremely relevant for assessing the ultimate-limit-state of the structures, these actions have been neglected here for the serviceability state. Secondly, some observations are yet to be compared against field measurements, and these, incorporated into models and simulations. Finally, albeit an extensive material characterisation campaign has allowed the study of relevant masonry types, the myriad of masonry configurations presents limits to these observations.

So, this paper details the three-tiered approach employed to quantify light damage in Dutch masonry structures exposed to induced earthquakes. First, experiments are used to get a glimpse into the light damage behaviour and calibrate finite element models capable of replicating masonry in terms of strength, stiffness, hysteresis and damage. Then, the models are extrapolated to simulate the impact of (repeated) seismic events and a relationship with light damage is established. Finally, this relationship is employed to compute the probability of light damage for different intensities of events. Yet, a first step is to define the nature of light damage.

2 Definition and quantification of light damage

It is difficult to characterise light damage without first defining it properly, and it is almost impossible to quantify its progression without having a precise denotation for it. Qualitative descriptions of damage are too vague to be able to monitor the progression of damage unless the damage increases significantly. It is thus necessary to measure damage based on a quantifiable measure. For aesthetic damage in masonry, cracks, an expression of damage, have been selected in this study to represent light damage. The width, length, and number of cracks in a masonry structure are used to monitor the progression of damage. The appearance of cracks is employed to define the initiation of the damage, and the ease of repair is utilised to categorise the damage. Such a classification, summarised in Table 1, has been adapted from earlier works by Boscardin et al. [10], Burland et al. [11], and, at its latest, Giardina et al. [12]. Three categories are represented with a light damage parameter using a single scalar. This parameter, called Ψ, summarises precisely, using Equation 1, the intensity of the damage, such that its initiation and progression can be

clearly monitored [16]. The parameter is related to the detectability and cost of repair of the damage; hence, wider cracks or a larger number of cracks are associated with a higher value of Psi. Mathematically, the parameter expresses the total of visible cracks such that the narrowest visible cracks with a width of 0.1 mm result in a value of around one (Ψ = l), slightly larger cracks of close to 1 mm width correspond to two (Ψ = 2) and cracks of approximately 4 mm in width give a value of three (Ψ = 3). The coefficients and exponents of Equation 1 have been tuned to adjust to this behaviour.

$$\psi = 2\, n_c^{0.15}\, \hat{c}_w^{0.3} \quad \text{with} \quad \hat{c}_w = \frac{\sum_{i=1}^{n_c} c_{w,i}^2\; c_{L,i}}{\sum_{i=1}^{n_c} c_{w,i}\; c_{L,i}} \tag{1}$$

Where n_c is the number of cracks in the wall or specimen, $\hat{c}_w$ is the width-weighted and length-averaged crack width (in mm) calculated with c_w (the maximum crack width along each crack in mm) and c_L (the crack length in mm). Hence, for n_c = l, $\hat{c}_w = c_w$. In this expression, the crack width of each crack is measured at their widest point. In this manner,

Table 1. Categorisation of light damage

Category	Damage		Description of typical damage and ease of repair	Approx. crack width
No damage (DS0)	negligible	Ψ = 0	No cracks	0
	invisible	Ψ < 1	Hairline cracks. Invisible to the naked eye.	< 0.1 mm
	just visible	Ψ ≥ 1	Fine cracks which can easily be treated during normal decoration.	> 0.1 mm
Aesthetic damage (DS1)	very slight	Ψ < 2	Perhaps isolated slight fracturing in building. Cracks in external brickwork visible on close inspection.	< 1 mm
	slight	Ψ ≥ 2	Cracks easily filled. Redecoration probably required. Several slight fractures showing inside of building. Cracks are visible externally and some repainting may be required externally to ensure water tightness.	> 1 mm
Moderate damage (DS2)		Ψ < 3		< 4 mm
	moderate	Ψ ≥ 3	Cracks difficult to fix, may require structural intervention.	> 4 mm

values of Ψ, lower than 1 correspond to cracks that cannot be seen with the naked eye, while when larger than 1, represent visible damage. This is herein marked as the initiation of light damage, and any increase in the Ψ parameter can be considered as progression of light damage.

3 Experimental tests for light damage

Experimental tests were performed on walls and spandrels. Both types of specimens were loaded in their plane and subjected to actions causing cracks in the range within light damage.

*3.1 **Wall tests***

The walls were single-wythe, 3 metres wide and 2.7 m tall, and most featured an opening for a window located asymmetrically. Figure 1 presents a drawing of the four types of walls while Table 2 shows an overview of all the specimens tested where all walls were loaded horizontally at the top. The clay walls were built using bricks in the format 50 x 100 x 210 mm, while the calcium-silicate walls used slightly larger bricks of 70 x 102 x 210 mm; both types of walls included a precast concrete window lintel with a height of one brick. The walls were subjected to a large number of cycles in order to investigate the progression of damage when exposed to repeated, identical solicitations. The large number of quasi-static cycles with small drift values were to mimic repeating seismic events causing light damage to the masonry (see number of steps and cycles, and their amplitudes in Table 2). Four types of walls were tested: fired-clay brick walls with an opening [17], similar calcium-silicate brick walls [18], clay masonry without an opening [19], and clay masonry with an opening and pre-damage [20]. The latter consisted of plastic strips positioned in specific joints so as to simulate an existing crack due to (previous) settlement actions. The walls were loaded with a constant vertical overburden so as to produce a vertical stress of 0.12 MPa in walls with an opening, and a higher stress of 0.46 MPa in the shear walls. The first value corresponds to one concrete- or two timber-floor storeys and a timber roof, and the latter to three concrete-floor storeys and a roof. This value is on the higher side, but was necessary to maintain reliable control of the test while enforcing a double-clamped condition, whereas for the walls with a window, a cantilever condition was employed.

Cracks were measured using Digital Image Correlation (DIC) and became visible at a lateral drift of approximately 0.25‰for both shear walls and walls with openings; both

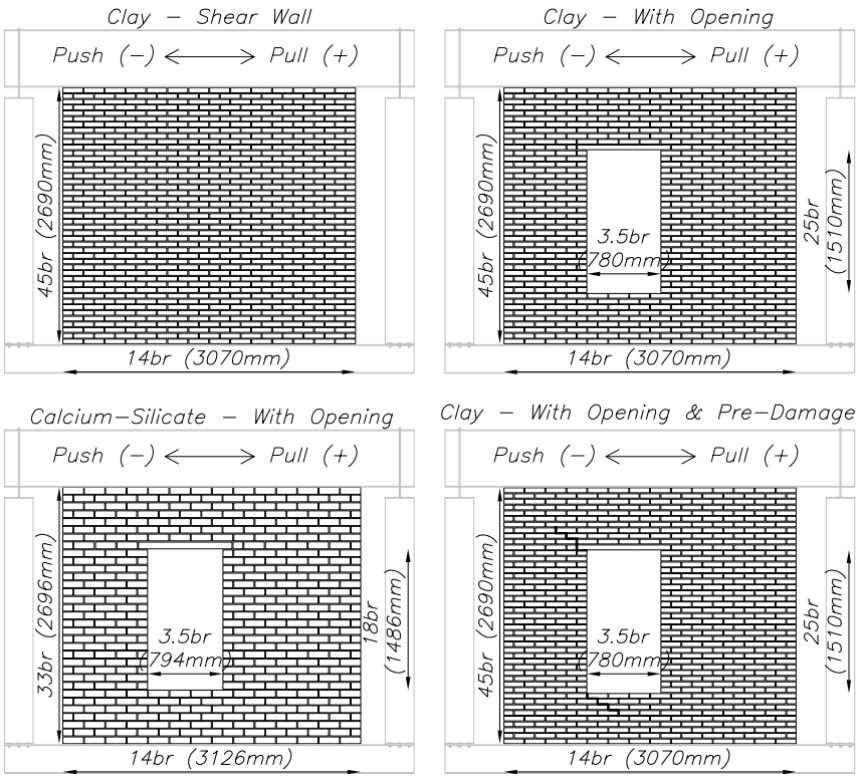

Figure 1. Drawings of the four types of wall specimens tested. Note: 'br' stands for 'bricks'.

Table 2. Overview of all walls tested for the light damage investigations

Wall iD	Wall Type	Description	Protocol	Steps & Boundary
TUD-Comp40	Clay with opening	First wall to be tested, few cycles.	5x3 one-way cyclic followed by 7x30 two-way cyclic	Drift (5): +0.26, +0.33, +0.41, +0.48, +0.55‰ Drift (7): ±0.26, ±0.33, ±0.41, ±0.48, ±0.55, ±0.63, ±0.70‰, Cantilever 0.12 MPa
TUD-Comp41		Identically-tested with a larger number of one-way cycles.	5x20 one-way cyclic followed by 7x30 two-way cyclic	
TUD-Comp42				
TUD-Comp43		The protocol was not quasi-static for the first part and the second part had a large number of cycles.	5x30 one-way cyclic (dynamic) followed by 7x50 two-way cyclic	
TUD-Comp44		Only one-way cycles tested because of error in control setup.	5x30 one-way cyclic	
TUD-Comp45	Clay with opening & pre-damage	Nominally-identical walls but including plastic strips in specific joints to simulate settlement pre-damage	5x30 one-way cyclic followed by 7x30 two-way cyclic	
TUD-Comp46				
TUD-Comp49	Calcium-Silicate with opening	Nominally-identical walls but built with calcium-silicate bricks.		
TUD-Comp50				
TUD-Comp47	Clay no opening	Shear walls tested in double-clamped condition with a high overburden.	6x10 asymmetric two-way cyclic	±0.27, ±0.33, ±0.42, ±0.49, ±0.59, ±0.70‰, Double-clamped 0.46 MPa
TUD-Comp48				

types of walls were tested to a drift of 0.7‰ where Ψ approached the upper boundary of what could be considered light damage. The cracks in the walls were mostly horizontal and diagonal following the masonry pattern and appeared at the interface between brick and mortar. At the later steps of the calcium-silicate walls however, the cracks also split bricks and cut vertically through these as depicted in Figure 2; this was not observed in any of the clay walls. Cracks grew in width and length not only when increasing the drift but also when the drift was kept constant. This occurred even when the drift was not reversed (one-way cyclic), but was more prominent during two- way cyclic tests. At the same time, the lateral force resisted by the walls (strength capacity) degraded approximately 5% over the first few cycles and stabilised towards the end of each step; this occurred after about 30 cycles and was thus selected as the typical cycle count in each step.

The initial crack pattern in the shear walls consisted of distributed stair-case diagonal cracks in the body of the wall, but consolidated into a single, wider diagonal crack towards the end of the tests. Conversely, the cracks in the walls with openings propagated from the four window corners, becoming longer and wider as the tests progressed. The pre-cracked joints in the pre-damaged walls only modified the crack pattern slightly but increased the intensity of the damage when compared to the virgin walls, especially at low values of drift, with up to 50% more damage on the first and second steps.

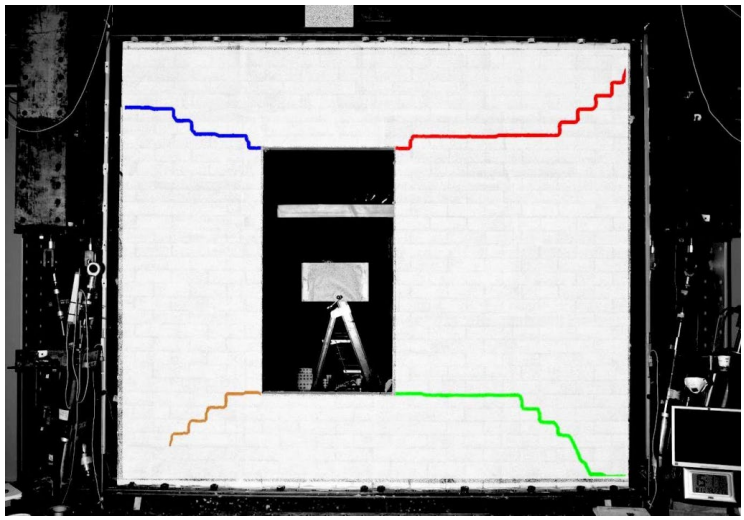

Figure 2. Calcium-silicate wall tested with final cracks highlighted. TUD-Comp50

The cracks were also assessed in order to establish a range for light damage from these experiments. A linear relationship was regressed between drift and the Ψ parameter for the different walls. Then, considering the limits presented in Table 1 and one standard deviation from the linear fit, lower and upper drift boundaries for light damage were determined; these are presented in Table 3.

Table 3. Summary of drift values for light damage from wall tests

	Clay brick		Calcium-silicate brick
	Flexural	Shear	Flexural
DS1 expected between	0.25‰	0.20‰	0.15‰
	1.10‰	0.90‰	0.65‰

3.2 ***Spandrel tests***

Similarly, spandrels of about 1.3 m in width and half a meter in height, were configured such that a vertical crack would develop. This was to replicate vertical cracks in masonry sometimes caused by earthquakes but predominantly triggered by settlement deformations. Moreover, the vertical crack in the spandrels and the horizontal and diagonal cracks in the walls, allowed for a more complete picture of the damage behaviour of the masonry material. The spandrels, as illustrated in Figure 3, were built of fired-clay and calcium-silicate bricks, and were loaded by two jacks (F) and supported by two rollers such that a vertical bending crack developed from the top-down. The development of this crack was guided by a sensor spanning the top three joints such that the crack mouth opening displacement (CMOD) was captured if any of the three joints was the one to crack.

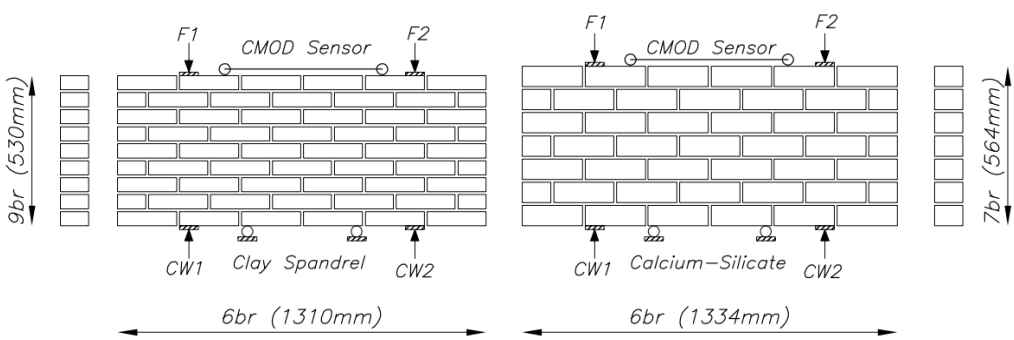

Figure 3. Spandrel and its loading scheme; fired-clay bricks (left) and calcium-silicate bricks (right)

Additionally, the tests could be performed cyclically by applying a constant counterweight force (CW) which acted against the force of the jack and allowed the loading direction to be reversed.

The two material variations of the spandrels were further varied by performing some tests monotonically and others cyclically with a different sequence of loading steps. These variations are summarised in Table 4. The monotonic tests increased the CMOD at a given rate, while the cyclic tests reached a certain displacement, returned to zero (limited by zero force), and repeated the same displacement for as many cycles as were in a step. The force required to attain a certain displacement dropped with each iterative cycle, with up to an approximate 20% average decrease in the last step. This strength degradation, also observed in the walls but at a reduced intensity, is presumably caused by sliding of the bricks at the bed joints. The vertical crack in fact, zigzagged down along the head- and bed-joints producing a toothed crack in the clay specimens. For the calcium-silicate samples however, the crack followed a straight vertical path cutting bricks in what was a brittle failure mechanism. When plotting the vertical displacements of the jacks against the force applied, the total energy input into the specimens and released by the vertical crack is displayed; then, the fracture energy can be computed for an idealised crack surface of 0.5 m in height and 0.1 m in width. This exercise is presented in Figure 4, where the aforementioned force versus displacement for a few representative tests is displayed; the fracture energy, G_f, is also included. This confirms that calcium-silicate tests behaved in a more brittle manner with a lower fracture energy, and verifies that the toothed crack observed in clay brick specimens allowed for a higher energy dissipation. It must be noted, however, that obtaining a fracture energy from cyclic tests is not correct and is presented here only as a comparison measure between the two materials.

Table 4. Overview of 29 spandrel tests

Spandrel Type	Number	Description	Protocol	Steps
Clay Monotonic	4	9 tests performed monotonically at two rates of CMOD control	Monotonic (0.5 µm/s)	CMOD (max. 10 mm)
	5		Monotonic (5 µm/s)	
Clay Cyclic	3	15 successful cyclic tests with clay specimens varying the number of steps and of cycles.	3x10 + monotonic	CMOD: 50, 100, 150 µm
	7		3x30 + monotonic	
	1		1x100 + monotonic	
	4		6x15 + monotonic	50, 70, 90, 110, 120,150 µm
Calcium-silicate Cyclic	5	Cyclic tests in calcium-silicate all with the best combination of steps and cycles	3x30 + monotonic	CMOD: 50, 100, 150 µm

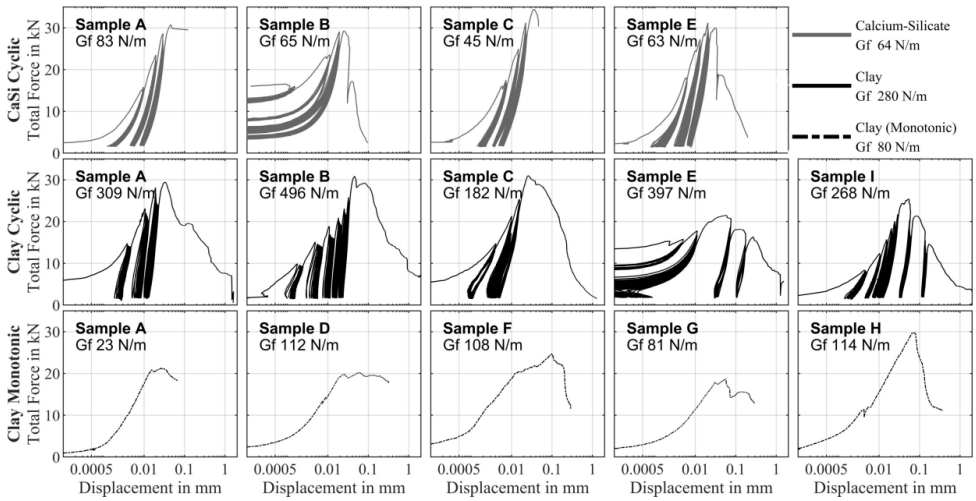

Figure 4. Total force against average logarithmic displacement of the jacks for a few tests. Note that this is not against the controlled CMOD. Values of average fracture energy shown include tests not plotted.

4 Calibration of finite element models

The experimental tests were reproduced with FE models using a non-linear material model to simulate the cracking behaviour of masonry. The orthotropic, total-strain based masonry model EMM (Engineering Masonry Model in DIANA FEA) was selected as constitutive model. This model includes different values of inelastic and elastic properties for the two main directions: the local x parallel to bed-joints and local y aligned with the head-joints. The in-plane crack directions are four: two of them are located along the joint's axes and the other two are diagonal, taking into account the masonry pattern by a parameter (angle for diagonal cracking). As failure mechanisms, the material model includes tensile cracking with softening and secant nonlinear unloading or reloading behaviour, Coulomb friction with cohesion softening and elastic unloading or reloading, and compression crushing (in both horizontal and vertical directions) with mixed secant or elastic unloading and reloading behaviour [13, 14]. The models employed a mesh size of 50 mm with quadrilateral 8-node quadratic elements (CQ16M) with 3 x 3 Gauss integration points.

The focus of the computations in this paper hereon will be on clay brick masonry; all clay specimens were modelled using the same set of properties for the material model, as they were also constructed from the same material. These material properties (detailed in Table

5) were partially selected from small companion tests such as bond-wrench tests, compression wallets, shear triplets and in-plane bending tests, and partially from the actual wall data. The calibrated values were varied within two standard deviations of the companion tests to assess their influence, but selected within one standard deviation to ensure a realistic set of properties. For example, the direct tensile strength, which is key for accurately determining the rocking and diagonal cracking behaviour, was varied between 0.1 and 0.2 MPa, ultimately selecting 0.16 MPa corresponding to the upper one-standard-deviation value from small scale tests. Two phases were used in the model: gravity and overburden were applied first, and the displacement field, yet not the stress field, was cleared. Then, the in-plane, displacement-controlled load was introduced in the model. The experimental protocol was employed but, in order to optimise the computational time, three cycles per step were considered as the material model does not yet include strength degradation and adding identical cycles would not have modified the results. Finally, the presence of plastic strips in the pre-damaged walls was simulated by modifying the material of the elements at the cracked positions with zero tensile strength.

Table 5. Properties and parameters used in the material model
Engineering masonry model, Clay masonry - Calibration

Material property	Unit	Value	Source
Density	kg/m³	1.62E+03	(1)
Elastic Modulus Perpendicular to Bed-Joints	MPa	3.57E+03	(1)
Elastic Modulus Parallel to Bed-Joints	MPa	2.50E+03	(1)
Elastic Shear Modulus	MPa	1.50E+03	(2)
Bed-Joint Tensile Strength	MPa	1.60E-01	(1)
Minimum Head-Joint Tensile Strength	MPa	1.60E-01	(2)
Tensile Fracture Energy	Nm/m²	1.13E+0l	(3)
Compressive Strength	MPa	1.29E+0l	(1)
Compressive Fracture Energy	Nm/m²	3.56E+04	(1)
Friction angle	rad	6.88E-01	(1)
Cohesion	MPa	1.70E-01	(1)
Shear Fracture Energy	Nm/m²	2.09E+02	(1)
Predefined Angle for Diagonal Cracking	rad	5.00E-01	(1)

(1) From experiments, (2) from calibration and (3) from formulation $G_{f,l} = 0.025(2\,ft)^{0.7}$

The calibration of the models was performed so as to obtain the most comparable behaviour in terms of initial stiffness, strength, and hysteresis, but also crack patterns and damage intensity. Figure 5 shows an example of a crack pattern comparison. The most influential parameters were the tensile strength of the masonry composite, the fracture energy, and the relationship between the head- and the bed-joint strength. The boundaries of the walls also played a significant role, especially for the double-clamped condition. Here, the two steel beams that supported, and to which the experimental walls were glued, were included in the models as elastic steel (ρ = 7.85 ton/m^3, E = 210 GPa, ν = 0.3) with a HEB-600 for the top and a HEB-300 line profiles for the bottom beam. The concrete lintel was modelled linear-elastically (ρ = 2.4 ton/m^3, E = 31 GPa, ν = 0.2). The flexural failure mechanism of windowed walls and the shear mechanism of squat walls was faithfully reproduced with the same model properties. This gives confidence that the models may be extrapolated to similar geometries while maintaining their veracity. Overall, the calibrated models can be described to be in good agreement with the experiments.

5 Extrapolation of FE models

5.1 Extrapolation models with walls

While the experiments consisted of quasi-static horizontal loads, the extrapolative models need to also consider dynamic loads with an additional vertical component. The calibrated models were thus modified slightly so as to input a seismic acceleration series and perform a non-linear time-history analysis (NLTHA). First, the steel beams were removed and, at the top, a line mass of 10 ton, simulating the presence of a floor was included, while, at the bottom, a set of springs and dampers was added to mimic the support of soil, silty sand or

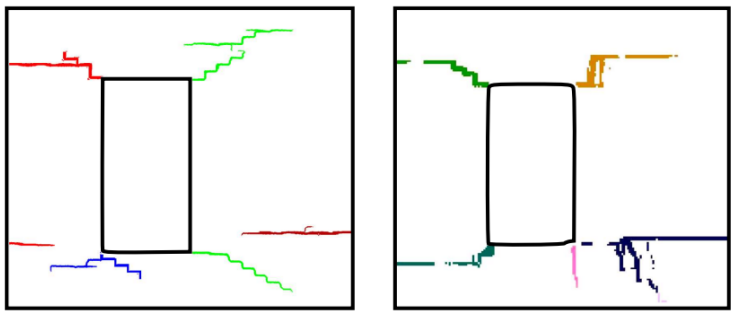

Figure 5. Comparison of detected crack pattern in the experiment of Comp46 (left) using DIC and the FE model of a clay wall with a window opening and pre-damage (right)

peat. The top mass had only a dynamic influence and did not modify the overburden on the wall of 0.12 MPa. The bottom interface was calibrated from other studies [9] and included, for the silty, sandy soil, a vertical stiffness modulus set to 0.44 N/mm^3 (0.57 N/mm^3 at the edges), and a constant horizontal stiffness of 0.38 N/mm^3. The vertical damping coefficient was 206 Ns/mm (6.87 Ns/mm at the edge), while the horizontal damping coefficient was set to 110 Ns/mm. A bad soil, consisting of peat, was also considered as comparison. Further, a Rayleigh damping of 2% based on the first two modes (for participating mass) was included in the dynamic models.

The accelerations corresponding to the earthquake of Zeerijp (8 January of 2018) registered on the surface stations (G-type [21]) of Garsthuizen and Appingedam, located 2.5 and 7.5 km from the epicentre respectively, were imposed at the base of the models. These two series were used to compare the response of the models when exposed to an earthquake recorded near the epicentre or far from the epicentre, respectively; both series were scaled to various values of peak ground velocity (PGV) starting at 2 mm/s (a PGA of 65 mm/s^2 approx.) considering the maximum rotated horizontal and its associated vertical component; the amplitude of the horizontal record was scaled to match the specified PGV while its vertical component was scaled with the same factor. Moreover, the response of the models was recorded after applying one or multiple, identical acceleration signals. An additional variation comprised the material, which modified its stiffness, tensile strength, and fracture energy to produce three sets of masonry: poor, standard, and strong, differing about 30% in tensile strength. Further, a vertical displacement profile was applied at the bottom edge of the wall's interface mimicking a hogging settlement profile with one edge

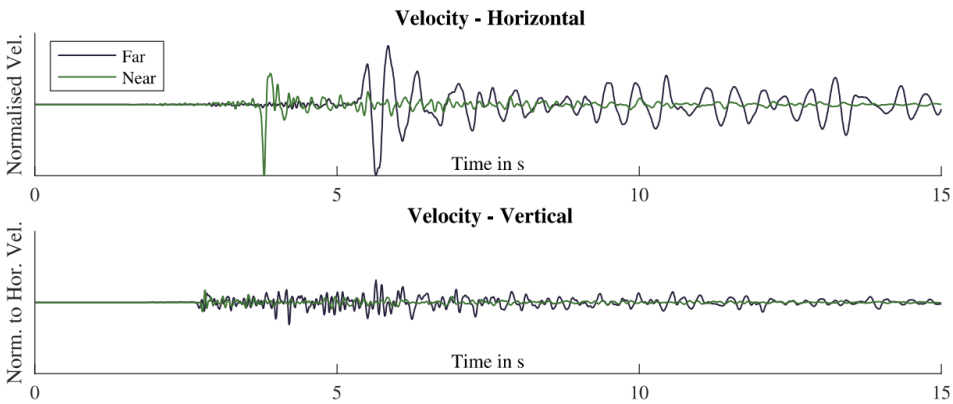

Figure 6. Normalised time series of peak ground velocity for the near and far stations

of the wall sinking deeper than the other. Depending on the magnitude of the settlement, the damage intensity of the wall, as measured with Ψ, varied between 0.5 and 1.5. Hence, unlike the calibration models were weakening of individual elements was applied to reproduce the experiments, for the extrapolation models, pre-damage was generated via pre-loading of the model. The various initial states of the models were then subjected to the imposed seismic accelerations.

In this manner, the relationship between, for instance, the initial damage or the number of seismic events and the final damage of the 2000 model permutations could be observed but, more importantly, quantified. First, expectedly, as the PGV increased, so did the final damage; after exposing some models to one earthquake of 8 mm/s, they exhibited an average damage increase of 0.20 Ψ, while at 16 mm/s, the increase was 0.36 Ψ (80% more) and at 32 mm/s, it was 0.57 Ψ (185%). When, however, they were exposed to two identical earthquakes of 8 mm/s, the average increase was 0.22 Ψ (10% more than one event); this shows that exposure to repeated earthquakes also leads to an increase in damage, albeit marginally so. Similarly, the average damage increase of the poor material was 34% higher than that of the standard material, while the stronger material was 24% less damaged on average. Additionally, models of walls starting with a low level of pre-damage ($\Psi_0 \approx 0.5$), obtained on average 12% less additional damage than completely virgin walls. This means that the initial damage helped mitigate the effect of the earthquake; note nonetheless, that the final damage value was higher than that of the virgin walls. Moreover, models of walls on peat accumulated 33% more damage than walls on the sandy soil; while, models of walls with a window attained a 25% higher increase in damage than walls without a window. And, models subjected to the record registered far from the epicentre of the earthquake displayed a 24% smaller increase in damage than those exposed to the signal recorded near the epicentre; note that both earthquakes were scaled to the same intensity and thus only the character of the record like frequency, effective cycles, and vertical acceleration, differ between them. Furthermore, the values described all refer to the increase in damage and not the final damage, as the pre- damaged models had differing initial values of damage.

5.2 *Extrapolation Models with Facades*

Four existing facades, identical to the ones used in the study of Van Staalduinen et al. [9] and taken from field-cases, were also modelled with an approach nominally identical to

the one described in section 5.1. The only significant variation concerned the lintels of the windows. As cracks are usually found around these openings, modelling of the lintel, especially for wider openings, is paramount. Three different lintel modelling approaches were followed depending on the width of the opening, just as in the field cases. For window or door openings narrower than one metre, no lintel is used and the masonry material is thus continuous in the model. For larger openings up to one and a half metres, a soldier lintel was considered consisting of vertical bricks; in the model, the local axes of the lintel portion was thus rotated. Finally, for larger openings, a steel beam was placed to hold the masonry such as is used in older structures; in the model, a Coulomb-friction interface is placed between the steel and the masonry. Moreover, for all facades, a masonry foundation, consisting of a thickening of the wall of 0.4 m was implemented and modelled with the non-linear material model with identical parameters as the rest of the facades.

The four facades were also subjected to settlement action producing an initial damage condition, exemplified in Figure 7a for facade 2, to compare against the undamaged condition. Then, the facades were analysed with similar permutations as the extrapolative wall models comprising variations in soil, in the masonry material, and in the intensity and distance (though not repetition) of the seismic events. An example of the final damage appraisal of the facade models is depicted in Figure 7b for facades 1, 3, and 4. This also illustrates the geometry of the four facades considered.

Damage was observed mostly around the openings, also in the top middle of openings without lintels, and at the edges of strong lintels when these were present. Cracks developed by the settlement action were further widened and lengthened by the imposed seismic accelerations. From these analyses, on average, the facades of poor material experienced 50% more increase in damage than the ones modelled with the standard material, whereas the strong material reduced the increase in damage by 25%. Similarly, the facades placed on the good, sandy soil displayed 13% less damage increase than those on the peat. Moreover, the facades with initial damage exhibited a 40% lower increase in damage than the ones with no initial damage; however, in all cases, the final damage of the pre-damage facades was higher. Furthermore, near earthquakes caused a 28% greater damage increase than earthquake of the far type; and, a PGV of 2 mm/s caused an average increase of 0.16 Ψ, with 4 mm/s leading to a 14% larger increase, 8 mm/s to 59% more, 16 mm/s caused 2.5 times the damage of a 2 mm/s event and 32 mm/s led to an average

increase of 0.70 Ψ (about 330% more than the lightest earthquake). Finally, at 32 mm/s, 4% of the initially undamaged models could be considered to have exceeded light damage, while, of the models with prior settlement damage, 9% exceeded light damage at 32 mm/s, 4% at 16 mm/s, and 2% at 8 mm/s.

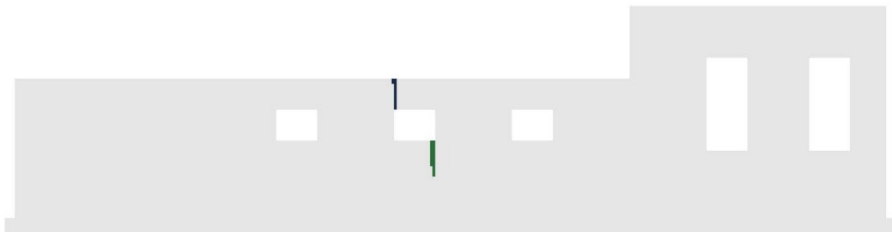

Figure 7a. Settlement damage of facade 2

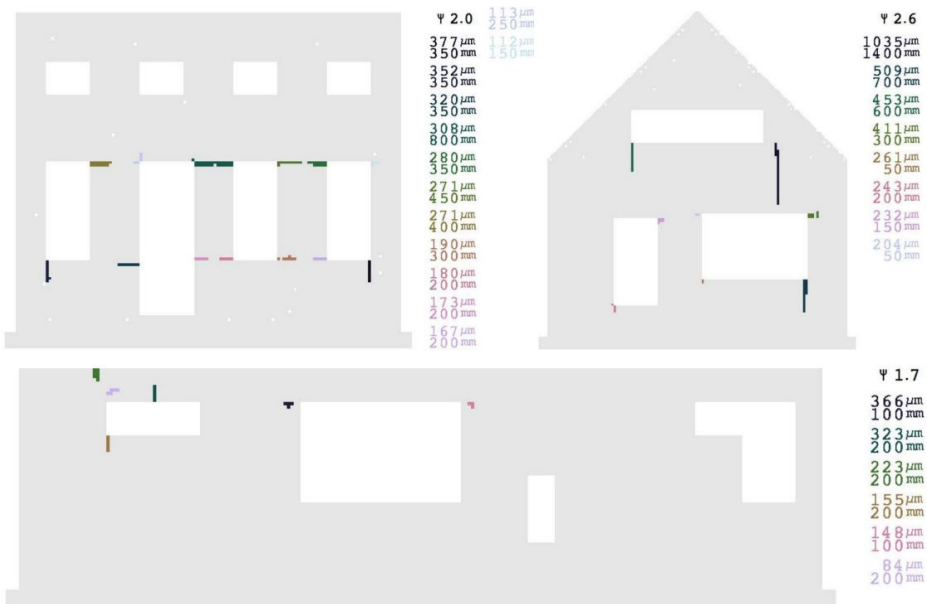

Figure 7b. Final damage of three different facades on peat, near earthquake, weak material, no pre-damage, and PGV of 32 mm/s. Top, left and right, facades 1 and 3; bottom, facade 4.

In comparison, the wall models of poor material appeared less vulnerable than the facades of poor material. Moreover, the larger and more complex facades also seemed more sensitive to larger PGVs than the walls, suggesting that the greater number of openings has a negative impact towards damage. In respect to soil type and distance to the epicentre, the walls produced results that are representative of the behaviour of the facades. In general, it

seems that the overall results of the wall models are in good agreement with the results obtained from the more complex facade models. In addition to the computations for clay brick reported herein, computational studies of the calcium-silicate masonry tests are currently being carried out, requiring extensions of the constitutive descriptions in order to capture the brittle splitting failures observed in the calcium-silicate bricks.

6 Earthquakes in Groningen and estimated light damage

The aforementioned wall models were employed to obtain a relationship between the final damage expressed in Ψ and various model parameters. A multi-variate regression model was fitted to the data such that the effect of each parameter combination could be represented. This model, briefly presented in the appendix, attained a good fit with a standard deviation of about 0.2 Ψ. This value was introduced as model uncertainty of the combined aspects of regression and finite element modelling. Further, each of the parameters was characterised with a probabilistic distribution. First, the material strength was varied according to results of companion tests [22], with a 30% variation for the material strength. Then, a rough spatial distribution of masonry structures in the seismic region was used to statistically determine a uniform probabilistic distribution for both the earthquake distance and the type of soil. The latter was coupled to a microzonation soil model [15], which, based on the shear wave velocity was used to classify soil as good (sandy) or bad (peat). Finally, an equal probability was given to the presence or absence of a window. Then, for different levels of initial damage and various intensities of earthquakes (measured in PGV), the probability of developing visible light damage was computed using a Monte Carlo simulation; these are summarised in Table 6. For the maximum intensity recorded to date (of approximately 32 mm/s), the probability of

Table 6. Probability of visible light damage ($\Psi \geq 0$)

PGV	No initial damage, $\Psi_0 = 0$	Light, yet imperceptible initial damage $\Psi_0 \approx 0.5$
5 mm/s	< 1%	2%
10 mm/s	1%	11%
15 mm/s	10%	33%
20 mm/s	20%	43%
30 mm/s	36%	57%
40 mm/s	51%	66%

developing visible light damage for these fired-clay masonry structures, lies between 40% and 60%.

The simulations also show a low probability of exceeding light damage ($\Psi \geq 2.5$) of 5% at 70 mm/s; however, since the models and analyses only consider in-plane damage and out-of-plane actions become more important at higher earthquake intensities, this value may be underestimated.

7 Conclusions

Experimental tests on fired-clay and calcium-silicate brick walls showed that visible cracks (or light damage), appear already at low in-plane drift values of 0.25‰. Moreover, the tests proved that these cracks will widen and lengthen when exposed to repeated identical actions. Additionally, the calcium-silicate walls appeared more vulnerable than clay masonry due to brittle, brick-splitting cracks. In the case of clay walls, these toothed vertical cracks give clay masonry a higher perceived fracture energy, meaning that computational models using continuum material models must consider the fracture energy to be orthotropic.

Furthermore, extensively calibrated models of the clay walls, with and without openings for windows, were extrapolated to assess seismic actions; these revealed that visible light damage is increased by repeated events, by prior existing damage of the structures, and by soft soils underneath. The relationships obtained between these parameters and light damage were then used to estimate the probability of damage at various peak ground velocity values: at 5 mm/s, the probability of clay walls displaying visible damage was negligible unless these already presented some unperceivable damage, in which case the probability reached 2%; similarly, at 10 mm/s, visible damage was pegged at 1% and 11% for walls with prior damage.

These estimations neglect out-of-plane actions under the premise that these are unimportant for light damage, but would be extremely relevant at higher earthquake intensities and more severe damage. Moreover, the investigations of this study have focused on single walls, and would benefit from experimenting on larger and more complex structures while also exploring additional material variations besides the fired-clay masonry representative of older structures and masonry veneers, and the calcium-

silicate brick masonry slowly offset by larger elements today. Finally, dynamic experiments and comparisons with more field-case data will help further validate the models and the observations drawn from them.

Acknowledgements

This research was funded by Nederlandse Aardolie Maatschappij (NAM) under contract number UI67339 'Damage sensitivity of Groningen masonry building structures - Experimental and computational studies', contract holders: Jan van Elk and Jeroen Uilenreef. This cooperation is gratefully acknowledged. The authors also express their gratitude to Edwin Meulman for his extensive support during the experimental phase.

References

[1] den Bezemer, T. & van Elk, J. (2018). Special Report on the Zeerijp Earthquake - 8th January 2018. NAM

[2] van Elk, J.F., Bourne, S.J., Oates, S.J., Bommer, J.J., Pinho, R. & Crowley, H. (2019). A Probabilistic Model to Evaluate Options for Mitigating Induced Seismic Risk. Earthquake Spectra · January 2019 DOI: 10.1193/050918EQS118M

[3] Messali, F., Esposito, R., Jafari, S., Ravenshorst, G., Korswagen, P.A. & Rots, J.G. (2018). A Multiscale Experimental Characterization of Dutch Unreinforced Masonry Buildings. 16th European Conference on Earthquake Engineering, Thessaloniki 2018

[4] Esposito, R., Messali, F., Ravenshorst, G.J.P., Schipper, H.R. & Rots, J.G. (2019). Seismic assessment of a lab- tested two-storey unreinforced masonry Dutch terraced house. *Bulletin of Earthquake Engineering* 17, 4601-4623 (2019). https://doi.org/10.1007/sl 0518-019-00572-w

[5] Graziotti, F., Tomassetti, U., Kallioras, S., Penna, A. & Magenes, G. (2017). Shaking table test on a full scale URM cavity wall building. *Bulletin of Earthquake Engineering*, 15 (12), pp. 5329-5364

[6] Didier, M., Abbiati, G., Hefti, F., Broccardo, M. & Stojadinovic, B. (2018). Damage Quantification In Plastered Unreinforced Masonry Walls Using Digital Image Correlation. 10th *Australasian Masonry Conference*, 14-18 February, 2018

[7] Godio, M., Vanin, F., Zhang, S. & Beyer, K. (2019). Quasi-static shear-compression tests on stone masonry walls with plaster: Influence ofload history and axial load ratio. *Engineering Structures* 192 (2019) 264-278

[8] Petry, S. & Beyer, K. (2015). Limit states of modem unreinforced clay brick masonry walls subjected to in-plane loading. *Bulletin of Earthquake Engineering* (2015) 13:1073-1095 DOI 10.1007/s10518-014-9695-9

[9] Van Staalduinen, P.C., Terwel, K. & Rots, J.G. (2018). Onderzoek naar de oorzaken van bouwkundige schade in Groningen Methodologie en case studies ter duiding van de oorzaken.. Delft University of Technology. Report number CM-2018-01, 11 July 2018 - Downloadable from www.NationaalCoordinatorGroningen.nl

[10] Boscardin, M.D. & Cording, E.J. (1989). Building response to excavation-induced settlement. *Journal of Geotechnical Engineering*, 115(1):1-21, 1989.

[11] Burland, J.B. & Wroth, C.P. (1974). *Settlement of buildings and associated damage. Proceedings of Conference on Settlement of Structures*, pages 611-654, Cambridge, 1974. Pentech Press.

[12] Giardina, G., van de Graaf, A.V., Hendriks, M.A.N., Rots, J.G. & Marini, A. (2013). Numerical analysis of a masonry fac;ade subject to tunnelling-induced settlements. *Engineering Structures* 54 (2013) 234-247

[13] Rots, J.G., Messali, F., Esposito, R., Jafari, S. & Mariani, V. (2016). Computational Modelling of Masonry with a view to Groningen induced Seismicity. *10th SAHC Structural Analysis of Historical Construction*, Leuven

[14] Schreppers, G.M.A., Garofano, A., Messali, F. & Rots, J.G. (2016). DIANA validation report for masonry modelling. DIANA FEA report 2016-DIANA-Rl601 TU Delft Structural Mechanics Report CM-2016-17, 143 pp

[15] Kruiver, P.P., van Dedem, E., Romijn, R., de Lange, G., Korff, M., Stafleu, J., Gunnink:, J.L., Rodriguez-Marek, A., Bommer, J.J., van Elk, J. & Doornhof, D. (2017). An integrated shear-wave velocity model for the Groningen gas field, The Netherlands. *Bulletin Earthquake Engineering* (2017) 15:3555-3580 - DOI 10.1007/sl0518-017-0105-y

[16] P.A. Korswagen & J.G. Rots (2020). Monitoring and quantifying crack-based light damage in masonry walls with Digital Image Correlation. *1st International Conference on Structural Damage Modelling and Assessment* (SDMA), Gent, Belgium 2020

[17] P.A. Korswagen, M. Longo, E. Meulman, J.G. Rots (2019). Crack initiation and propagation in unreinforced masonry specimens subjected to repeated in-plane loading during light damage. *Bulletin of Earthquake Engineering* (2019) 17:4651--4687 doi.org/10.1007/sl0518-018-00553-5

[18] P.A. Korswagen, M. Longo, J.G. Rots (2020). Calcium silicate against clay brick masonry: an experimental comparison of the in-plane behaviour during light damage. *Bulletin of Earthquake Engineering* (2020) 18:2759- 2781 doi.org/10.1007/sl 0518-020-00803-5

[19] P.A. Korswagen, M. Longo, J.G. Rots (2020). High-resolution monitoring of the initial development of cracks in experimental masonry shear walls and their reproduction in finite element models. *Engineering Structures* 211 (2020) 110365 doi.org/10.1016/j.engstruct.2020.110365

[20] P. Korswagen, M. Longo, E. Meulman, J.G. Rots (2019). Experimental and Computational Study of the Influence of Pre-Damage Patterns in Unreinforced Masonry Crack Propagation Due to Induced, Repeated Earthquakes. *13th North American Masonry Conference*, Utah, USA 2018

[21] KNMI Seismic & Acoustic Data Tools - rdsa.knmi.nl -Acquired January of 2020.

[22] Jafari, S., & Esposito, R. (2017). Material tests for the characterisation of replicated solid clay brick masonry. Delft University of Technology.

Appendix - Physical regression model

The results of FE wall modes were reproduced with a regression model based on physical observations between parameters, see Figure 8. The model equations and its regression coefficients were adjusted such that the following physical observations were embodied: 1) The higher the PGV, the more damage is expected; 2) The higher the pre-damage value, the higher the final damage. However, the difference between initial damage and final damage diminishes when the initial damage is higher; 3) The weaker the material, the higher the final damage; 4) The more flexible soil (B) leads to lower damage. Note that the amplification that bad soils produce is not considered here since the PGV is being used directly; 5) The more flexible facade (A) shows higher damage for the near earthquake, while the rigid facade shows more damage for the far earthquake; and, 6) The larger the number of earthquakes, the higher the final damage.

The final value of damage is equal to the initial damage value (ψ_0) plus a damage increase ($\Delta\psi$), see Equation 2. The increase in damage is always equal or larger than zero and is a function of PGV as a combination of logistic and linear components (Eq. 3).

$$\psi_f = \psi_0 + \Delta\psi \tag{2}$$

$$\Delta\psi = \beta_1\left(\frac{1}{1+e^{\beta_2}} + \beta_3\right) + \varepsilon \geq 0 \tag{3}$$

Where ε is the model uncertainty parameter, β_1 is the scaling factor in the function, β_2 is the exponent of the logistic component and β_3 is the linear component; these three are in tum defined as:

$$\beta_1 = \frac{\alpha_1 N^{\alpha_2}}{1+\psi_0^{\alpha_3}} \tag{4}$$

$$\beta_2 = 5 - \frac{\frac{1}{2}\mathrm{PGV}}{1+\alpha_4\,\psi_0^{\alpha_5} + \alpha_8\, m^{\alpha_9}} \tag{5}$$

$$\beta_3 = \frac{\mathrm{PGV}}{1+\alpha_6\,\psi_0^{\alpha_7} + \alpha_{10}\, m^{\alpha_{11}}} \tag{6}$$

Where N is the number of consecutive, identical events, m is the normalised material strength given by the ratio of tensile strength over the tensile strength of the standard material, and α are the eleven regression coefficients. Their values are gathered in Table 7

for each of the eight combinations of binary variables. The model outputs a mean of 0.17 Ψ between the fit and the data points; hence, ε was assumed to be normally distributed with a standard deviation of 0.2 to account for both the imperfect fit of the regression model and the epistemic uncertainty in the FE models.

Table 7. Summary of regression coefficients. Combinations of soil (A or B), facade (A or B) and earthquake type (Near or Far). The highlighted row is visualised in Figure 8.

Combi.	Coefficients											Abs. Residuals	
	α1	N	Ψ_0 Pre-damage					m Material					
		α2	α3	α4	α5	α6	α7	α8	α9	α10	α11	Mean	σ
A-A-Ne	0.64	0.15	1.55	0.34	6.24	3E-12	6E-07	1E-12	1E-10	35.21	1.08	0.14	0.15
A-A-Fa	0.42	0.02	1.70	0.01	71.77	1E-12	2.78	0.73	0.99	29.05	0.83	0.09	0.10
A-B-Ne	0.58	0.11	2E-11	6E-04	11.26	1E-11	0.04	0.05	7.43	71.10	1E-12	0.19	0.19
A-B-Fa	0.31	0.23	1E-12	1E-12	2E-05	1E-12	2E-12	1.49	1E-12	26.83	2E-11	0.26	0.26
B-A-Ne	0.64	0.18	1.38	0.36	6.00	1E-12	2E-04	2E-04	7.04	34.61	1.09	0.13	0.16
B-A-Fa	**0.42**	**0.04**	**1.55**	**0.05**	**100.00**	**3E-07**	**0.57**	**0.60**	**2.99**	**28.09**	**0.88**	**0.11**	**0.11**
B-B-Ne	0.62	0.21	0.84	4E-05	23.33	3E-03	1.23	4E-04	28.56	80.31	1.30	0.18	0.17
B-B-Fa	0.36	0.25	0.04	3E-05	22.85	6E-04	0.06	1.51	1.75	31.73	0.34	0.25	0.27
												0.17	0.06

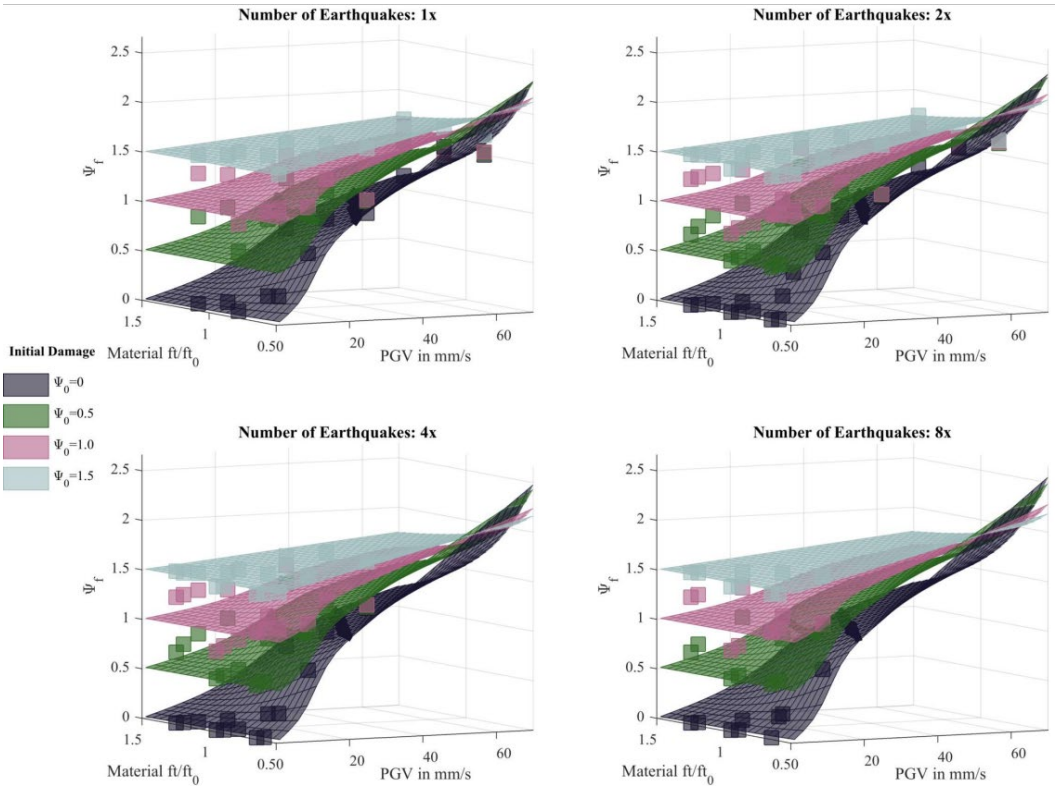

Figure 8. Data points from the extrapolation models on bad soil (B) for the facade with a window (A) and for far earthquakes (Fa), with the fitting curves from the physical regression model developed. Most damage occurs for the weak material subjected to high PGV values.